Eur. Phys. J. D (2015) 69: 135
DOI: 10.1140/epjd/e2015-50875-3

THE EUROPEAN PHYSICAL JOURNAL D

Regular Article

A sensitive and accurate atomic magnetometer based on free spin precession

Zoran D. Grujić[1,a], Peter A. Koss[1,b], Georg Bison[2], and Antoine Weis[1]

[1] Physics Department, University of Fribourg, 1700 Fribourg, Switzerland
[2] Paul Scherrer Institute, 5232 Villigen, Switzerland

Received 5 December 2014 / Received in final form 17 March 2015
Published online 21 May 2015 – © EDP Sciences, Società Italiana di Fisica, Springer-Verlag 2015

Abstract. We present a laser-based atomic magnetometer that allows inferring the modulus of a magnetic field from the free Larmor precession of spin-oriented Cs vapour atoms. The detection of free spin precession (FSP) is not subject to systematic readout errors that occur in phase feedback-controlled magnetometers in which the spin precession is actively driven by an oscillating field or a modulation of light parameters, such as frequency, amplitude, or polarization. We demonstrate that an FSP-magnetometer can achieve a ∼200 fT/$\sqrt{\text{Hz}}$ sensitivity (<100 fT/$\sqrt{\text{Hz}}$ in the shotnoise limit) and an absolute accuracy at the same level.

1 Introduction

The past decade has witnessed the development of a wealth of atomic magnetometer methods deploying laser-based preparation and readout of precessing spin polarization in paramagnetic atomic vapours/gases [1]. Applications of atomic magnetometers cover the detection of magnetic fields of biological origin, such as in magnetocardiography [2,3] and magnetoencephalography [4], the detection of ultralow-field NMR [5] and ultralow-field MRI [6] as well as the monitoring of fields in fundamental symmetry experiments [7]. Most of those applications call for magnetometers with the highest possible sensitivity, i.e., the best capability to detect small magnetic field changes, where the absolute precision and accuracy of the field determination are of secondary importance.

Our team is involved in a large collaborative effort [8] searching for a permanent electric dipole moment of the neutron (nEDM experiment). In that experiment an array of Cs vapour magnetometers monitors the spatial and temporal stability of a 1 μT magnetic field applied to an ensemble of ultracold neutrons, a task, for which both sensitivity and accuracy are primary issues. The magnetometers use optically detected magnetic resonance (MR) in the so-called M_x-geometry, in which the frequency of a weak oscillating magnetic field is actively kept in resonance with the atomic spin precession at the Larmor frequency [9,10]. Although a frequency measurement is an intrinsically very precise metrological technique, it suffers from the fact that small errors of the feedback signal's phase yield systematic frequency shifts that may be orders of magnitude larger than the intrinsic magnetometer sensitivity.

Here we report on a magnetometer approach, in which an initially spin-polarized sample of Cs vapour atoms is allowed to freely precess (and decay) at the Larmor frequency in the magnetic field of interest. The free spin precession (FSP) of the atomic spin-polarization is recorded by a weak intensity probe laser beam that affects the FSP process in a minimal way. FSP magnetometry avoids systematic readout errors of feedback-driven magnetometer schemes, while maintaining all advantages associated with performing the field measurement in terms of a frequency measurement, thus offering the potential for a field determination with both high sensitivity and high accuracy.

2 FSP magnetometry

The first recording of an optically detected FSP signal in an atomic vapour was reported by Dehmelt [11] in 1957 who showed that the optical absorption coefficient of an atomic vapour is modulated by precessing polarized spin 1/2 atoms. Kukolich [12] extended the work of Dehmelt to spin 1 and spin 2 atoms. In more recent times pump-probe experiments recording the FSP of atomic (electronic) spin polarization were used to study collisional dynamics and light shifts in alkali vapours [13,14].

FSP signals have been deployed for specific magnetometry tasks using (nuclear) spin-polarized mercury atoms [15] and ^{3}He atoms [16,17], or (electronic) spin-polarized alkali atoms [18–20]. The good signal to noise ratio and simplicity of its implementation makes the FSP

[a] e-mail: zoran.grujic@unifr.ch
[b] *Present address:* Instituut voor Kern- en Stralingsfysica, Katholieke Universiteit Leuven, B3001 Leuven, Belgium.

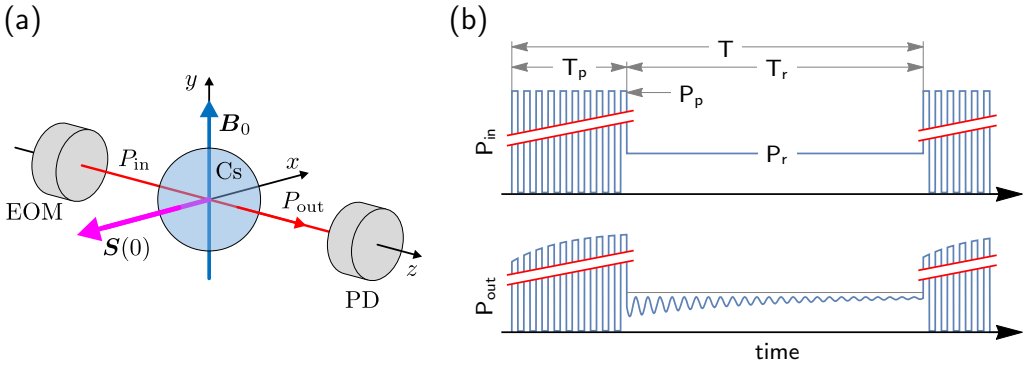

Fig. 1. (a) Geometry of the magnetically-silent FSP magnetometer. (b) One measurement cycle of duration T. The spin polarization is created by amplitude-modulated light with peak power P_p during a pumping time T_p, following which the FSP signal is recorded by a weak readout beam during a time T_r at constant power P_r. The top graph represents the laser power before the cell and the lower graph represents the transmitted light power detected by the photodiode (PD). Note that the power and frequency are not presented to scale for clarity.

technique based on atomic alignment (i.e., using linearly polarized light) a useful tool for the easy calibration of magnetic coils [21], or for measuring the magnetic field orientation and modulus [20]. Recently an FSP magnetometer using nuclear-spin-polarized ^{3}He gas was reported claiming a relative precision $\Delta B_0/B_0$ below 10^{-12} for the determination of fields $B_0 > 100$ mT [16].

The FSP magnetometer described hereafter is "magnetically silent", in the sense that its operation does not require the application of an oscillating magnetic field to the sensor cell. This offers a certain advantage when the magnetometer is to be operated in harsh environments, such as in high vacuum and/or in proximity of a high voltage electrode, such as in the mentioned EDM experiment [8].

3 Experiments

3.1 Apparatus

Figure 1a shows the layout of the magnetometer. The experiments were performed in Cs vapour using light from a single mode diode laser whose frequency is actively stabilized to the $4 \rightarrow 3$ component of the Cs D_1 transition by means of Doppler-free saturation spectroscopy. The laser light is carried to the spectroscopy cell by an optical fiber with an integrated electro-optic modulator, EOM (model AM905 from Jenoptik) that allows the electronic control of the laser power. Prior to entering the cell the light emerging from the fiber is collimated to a beam of ∼4 mm diameter that is made circularly polarized by a polarizer and a $\lambda/4$-plate. A photodiode with a radiant sensitivity of ∼0.54 μA/μW (∼75% quantum efficiency) placed after the cell detects the transmitted laser power. Cesium vapour with a saturated vapour pressure at room temperature is contained in a 30 mm diameter paraffin-coated Pyrex cell [22]. The cell is exposed to a homogeneous magnetic field B_0 of ∼1 μT, produced by a solenoid, and oriented at 90° with respect to the light's propagation direction $\hat{k}$. The sensor cell, solenoid and photodetector are mounted inside of a multi-layer μ-metal shield.

3.2 Recording FSP signals

A measurement cycle of duration T consists of a pump (preparation) phase of duration T_p, followed by a readout (probe) phase of duration T_r (Fig. 1b). During the pump phase atomic spin polarization is created by optical pumping with the circularly-polarized beam. Since optical pumping by cw light in a (polarization destroying) transverse magnetic field is not very efficient, we use the synchronous amplitude modulation method introduced by Bell and Bloom in 1961 [23]. That method was recently extended to excitation by an intensity-modulated laser beam combined with phase-sensitive detection [24–26]. In Bell-Bloom pumping the light intensity is modulated from "on" to "off" state by means of the EOM driven by a square wave of duty cycle η, meaning $t_{on}/t_{off} = \eta/(1-\eta)$, producing a peak power P_p. The modulation frequency is chosen to coincide with the Larmor precession frequency of the spin polarization around the transverse field $\boldsymbol{B}_0$. The Larmor frequency of the $F_g = 4$ Cs ground state is given by $\omega_L = \gamma_4 |\boldsymbol{B}_0|$ where $\gamma_4/(2\pi) \approx 3.50$ Hz/nT is the corresponding gyromagnetic ratio. After the preparation cycle the light power is lowered to a constant (i.e., unmodulated) value P_r that is sufficiently weak, so that it does not induce significant optical pumping (Fig. 1). The time dependent photodiode signal during this readout phase constitutes the signal of interest. The readout signal is recorded with 16 bit vertical resolution by a digital USB oscilloscope (model HS5 from TiePie engineering) sampling the photodiode signal at a rate of 6.25 MHz. It has the generic shape of a damped oscillation, and the extraction of its oscillation (i.e., Larmor) frequency by post-processing of the data allows the determination of the magnetic field. The method is similar to the method described by Jensen [27].

4 FSP signal modeling

The build-up of spin orientation by an intensity-modulated laser beam was discussed by Grujić and Weis [26]. The FSP signal originates from the fact that the absorption coefficient of the atomic medium depends on the degree and orientation of its spin polarization $\boldsymbol{S}$. The explicit time dependence of the transmitted laser power depends on $\hat{k}\cdot\boldsymbol{S}(t)$, i.e., on the projection of the polarization onto the light propagation direction $\hat{k}$.

We model the spin polarization as a vector polarization (orientation) $\boldsymbol{S}$ that is proportional to $\langle\boldsymbol{F}\rangle$, $\boldsymbol{F}$ being the total angular momentum operator. Optical pumping with circularly polarized light produces also a tensor polarization (alignment) oriented along $\hat{k}$. However, it is known that alignment contributions are very small on the Cs $4\rightarrow 3$ transition of the D_1 line [26]. Moreover, alignment contributions to the FSP signal will manifest themselves as oscillations at $2\omega_L$ only (for $\hat{k}\cdot\hat{B}_0=0$) that can easily be discriminated by filtering.

Neglecting alignment contributions we can model the FSP dynamics by time-dependent solutions of the Bloch equations for the spin orientation vector $\boldsymbol{S}$

$$\dot{\boldsymbol{S}}=\boldsymbol{S}\times\boldsymbol{\omega}_L-\gamma\boldsymbol{S}+\gamma_r\left(\boldsymbol{S}_{\hat{k}}-\boldsymbol{S}\right), \tag{1}$$

where γ is the polarization relaxation rate (assuming equal longitudinal γ_1 and transverse γ_2 rates [28,29]). The last term in equation (1) takes the production of spin polarization by optical pumping (at a rate γ_r) with the low power readout beam into account. The spin orientation $\boldsymbol{S}_{\hat{k}}$, parallel to $\hat{k}$, would be reached asymptotically by optical pumping if there was no relaxation in the system, i.e. $\gamma=0$.

We choose $\boldsymbol{B}_0=B_0\,\hat{e}_y$ and $\hat{k}=\hat{e}_z$ (cf. Fig. 1a) and solve the Bloch equations (1) with the boundary condition $\boldsymbol{S}(t=0)=-S_0\,\hat{e}_x$. The solution for the polarization component along the light propagation direction is given by

$$S_z(t)=a_c\left(1-e^{-\Gamma t}\cos\omega_L t\right)+a_s\,e^{-\Gamma t}\sin\omega_L t, \tag{2}$$

where the damping rate γ is affected by residual optical pumping (at rate γ_r) by the readout beam according to

$$\Gamma=\gamma+\gamma_r. \tag{3}$$

To first order in γ_r/γ, the oscillation amplitudes are given by

$$a_c=\frac{\gamma}{\omega_L^2+\gamma^2}\,\gamma_r\quad\text{and}\quad a_s=\frac{\omega_L}{\omega_L^2+\gamma^2}\,\gamma_r+S_0, \tag{4}$$

which reduce to

$$a_c\approx\frac{\gamma_r}{\gamma}\,\frac{1}{Q^2}\quad\text{and}\quad a_s\approx\frac{\gamma_r}{\gamma}\,\frac{1}{Q}+S_0, \tag{5}$$

in the high-Q limit, where $Q=\omega_L/\gamma$.

Following the discussion in references [28,29] the power of a circularly polarized light beam transmitted by an optically thin ($\kappa_0 L\ll 1$) ensemble of polarized atoms is given by

$$P(t)\approx P_0(1-\kappa_0 L)+P_0\kappa_0 L\alpha_{43}^{(1)}S_z(t), \tag{6}$$

where κ_0 is the optical absorption coefficient of the unpolarized ensemble ($S_z=0$) at the peak of the Doppler-broadened $4\rightarrow 3$ transition, and where the constant $\alpha_{43}^{(1)}$ is a hyperfine transition specific orientation analyzing power [28,29].

Inserting (2) into (6) then yields a time dependent photocurrent of the general form

$$I(t)=I_{DC}+\left(I_c\cos\omega_L t+I_s\sin\omega_L t\right)\,e^{-\Gamma t}. \tag{7}$$

The last equation has to be modified in order to take hyperfine relaxation into account. In fact, at the end of the pumping cycle, a substantial population of atoms has transferred to the $F_g=3$ hyperfine ground state that is not coupled to the light field therefore reducing the population N_4 on the $F_g=4$ state to the value N_{4p}. At the end of the weak light probing period a new equilibrium will be established with population N_{4r}. The light absorption is proportional to $\kappa_0(t)=N_4(t)\,\sigma_{4\rightarrow 3}$, where $\sigma_{4\rightarrow 3}$ is the light absorption cross section leading to a change of light absorption during the probing period with relaxation rate γ_{hf} between two hyperfine ground sates. The relaxation mechanism can be modeled empirically by

$$N_4(t)=N_{4r}-\left(N_{4r}-N_{4p}\right)e^{-\gamma_{hf}t}, \tag{8}$$

where t refers to the readout process starting at $t=0$. As a consequence, the time-dependent power will have the general form

$$I(t)=I_{DC}+I_{hf}\,e^{-\gamma_{hf}t}+\left(I_c\cos\omega_L t+I_s\sin\omega_L t\right)\,e^{-\Gamma t}. \tag{9}$$

5 Data analysis and system optimization

Figure 2a shows a raw experimental FSP trace (expressed in terms of the photodiode current) that was obtained under optimized experimental conditions in a field B_0 of 1 μT. The Fourier transform of that signal (Fig. 2b) shows resonances at $\nu_L\sim 3.5$ and $2\nu_L\sim 7$ kHz, that represent the FSP of the orientation (ν_L) and alignment (ν_L and $2\nu_L$). The DC offset and the slowly decaying background from equation (9) are represented by the resonance at 0 Hz.

In order to isolate the signal of interest at ω_L we filter the raw data (in time space) by a numerical band-pass filter that removes low frequency components (drift of the laser power, exponential decay from hyperfine relaxation) and the alignment contribution at $2\omega_L$, yielding the cleaned-up FSP signal shown in Figure 2c. The filter is a finite impulse response band pass that we have described earlier [21]. The filter's transfer function in the frequency

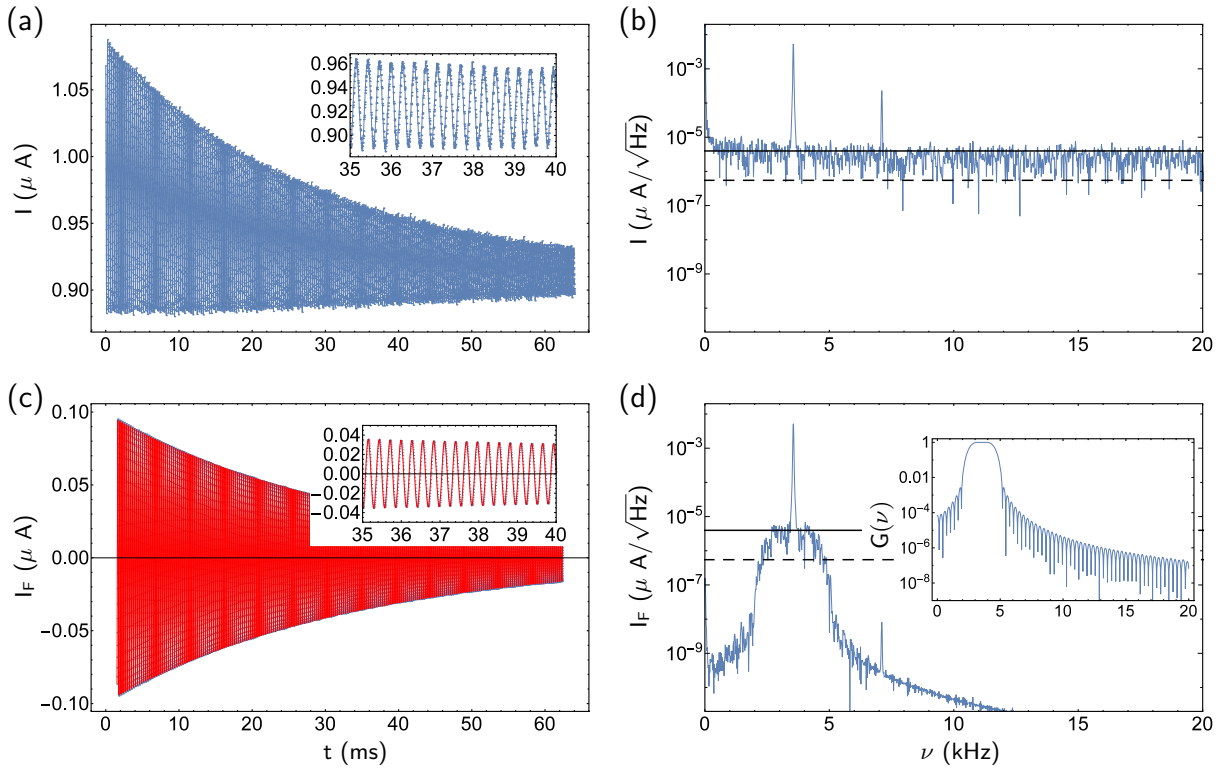

Fig. 2. (a) Typical FSP time series (raw data) in a 1 μT magnetic field recorded by a digital oscilloscope with 16 bit vertical resolution at a 200 kHz sample rate. The inset shows 5 ms of data from the middle part of the signal. The solid line is drawn to guide the eye. (b) FFT of the data from (a) showing oscillations at $\omega_L/(2\pi) \sim 3.5$ kHz and $2\omega_L$ caused by precessing orientation and alignment. (c) FSP signal after offline digital filtering (in time space) by a finite response bandpass filter. The solid line represents a fit of the data by the function (11). (d) FFT of the filtered signal in (c), with inset showing the transfer function of the finite response filter $G(\nu)$. In both FFT graphs (b,d), the solid and dashed lines represent the average white noise level of 4.0 pA/$\sqrt{\text{Hz}}$ near the orientation resonance and the photon shotnoise level of 0.55 pA/$\sqrt{\text{Hz}}$, respectively.

domain (see inset of Fig. 2d) is given by

$$G(\nu) = \frac{1}{2}\left[\text{erf}\left(\frac{\nu - \nu_c + \delta\nu}{\beta}\right) + \text{erf}\left(\frac{\nu + \nu_c + \delta\nu}{\beta}\right) - \text{erf}\left(\frac{\nu - \nu_c - \delta\nu}{\beta}\right) - \text{erf}\left(\frac{\nu + \nu_c - \delta\nu}{\beta}\right)\right], \tag{10}$$

where ν_c (set to ν_L), $\delta\nu$, and β represent the filter's center frequency, its spectral width, and the steepness of its edges, respectively.

The precession frequency ω_L, the damping rate Γ and the FSP amplitude are obtained by fitting the function

$$I_F(t) = (I_c \cos\omega_L t + I_s \sin\omega_L t)\, e^{-\Gamma t}, \tag{11}$$

to the filtered data. The FSP amplitude is then $I_0 = \sqrt{I_c^2 + I_s^2}$. We found that the use of the fit function (11) is computationally less power demanding and yields more stable fit results than the equivalent simpler expression $I_F(t) = I_0 \sin(\omega_L t + \varphi)\, e^{-\Gamma t}$ with $\tan\varphi = I_c/I_s$.

5.1 Cramér-Rao lower bound for the standard deviation of ω_L

The statistical precision with which the frequency ω_L can be extracted from the recorded time series can be expressed by σ_ω. Estimation theory allows expressing the lower bound for σ_ω – known as Cramér-Rao lower bound (CRLB) [30,31] – in terms of experimentally measurable parameters.

The FSP time series consists of discrete data points (photocurrent values)

$$i(n) = I_0 \cos(\omega_L\, n\Delta t + \varphi)\, e^{-\Gamma\, n\Delta t} + w(n), \tag{12}$$

that are recorded by a digital oscilloscope, where $w(n)$ represents white Gaussian noise, and where the sampling interval Δt is the inverse of the sampling rate. An unbiased frequency estimator, assuming constant B_0 and Gaussian noise, can determine the frequency of a single FSP trace with an uncertainty $\sigma_f = \sigma_{\omega_L}/(2\pi)$ that is no better than

$$\sigma_f \geq \frac{\sqrt{12}}{(I_0/\rho_I)\; T_r^{3/2}}\, C, \tag{13}$$

where I_0/ρ_I is the signal to noise ratio (SNR), ρ_I being the photocurrents's spectral noise density at the resonance

frequency. T_r is the length and $N = T_r/\Delta t$ the number of data points of the time series. The correction factor C is unity for an undamped sine wave, while for a decaying signal it is given by

$$C = \frac{N^3}{12} \frac{\left(1-z^2\right)^3 \left(1-z^{2N}\right)}{z^2\left(1-z^{2N}\right)^2 - N^2 z^{2N}\left(1-z^2\right)^2}, \qquad (14)$$

where $z = e^{-\Gamma \Delta t}$ [32]. Note that C strongly depends on Γ and T_r while its dependence on N is negligible for a reasonably high sample rate $1/\Delta t$.

The standard deviation σ_f translates into a lower bound for the statistical uncertainty of the field determination from a single FSP by

$$\sigma_{B_0} = \frac{\sigma_{\omega_L}}{\gamma_F} = \frac{\sigma_f}{2\pi\,\gamma_F}. \qquad (15)$$

Since an FSP cycle requires a total time $T = T_p + T_r$, the measurement bandwidth is given by $f_{\rm bw} = 1/(2T) = 1/2\,(T_p + T_r)^{-1}$. Assuming white noise, σ_{B_0} can be converted to a noise density

$$\rho_{B_0} = \frac{\sigma_{B_0}}{\sqrt{f_{\rm bw}}} = \sigma_{B_0}\sqrt{2T}, \qquad (16)$$

which measures the magnetometer sensitivity independent of the bandwidth $f_{\rm bw}$.

5.2 Optimizing experimental parameters

We characterize the FSP magnetometer's sensitivity in terms of ρ_{B_0} which has the unit $\mathrm{T}/\sqrt{\mathrm{Hz}}$. Equation (13) shows that the magnetometric sensitivity depends on the signal to noise ratio I_0/ρ_I, the factor C, and the total FSP recording time T. Each of these quantities depends in a non-trivial way on the experimental parameters of the pump process, viz., P_p (the peak pump power), η (the duty cycle of the pulsed pump process, and T_p (the pump process duration) as well as the parameters of the probe process, viz., P_r (the readout power, characterized by I_{DC}, the DC photocurrent) and T_r (the FSP recording time). We have carried out a systematic study of the dependence of ρ_{B_0} on those parameters.

The FSP amplitude I_0 is a function of T_p, P_p, η and the residual polarization of the medium at the moment when pumping was started. Figure 3 shows the dependence of I_0 on the pumping time T_p. The readout duration T_r was chosen to be several relaxation periods long, so that the ground state sublevel populations have fully thermalized before the following pump pulse train. The scattering of the data for $T_p > 100$ ms is most likely due to laboratory temperature, i.e. Cs density variations. The dashed line represents a fit of the data with $A = a(1-e^{-\gamma_p T_p})$, yielding a pump rate (during the pump process proper) of $\gamma_p = 2\pi 22$ Hz. The overshoot of the data near $T_p \sim 50$ ms is probably due to the loss of atoms in the $F_g = 4$ state by hyperfine pumping to the uncoupled $F_g = 3$ state.

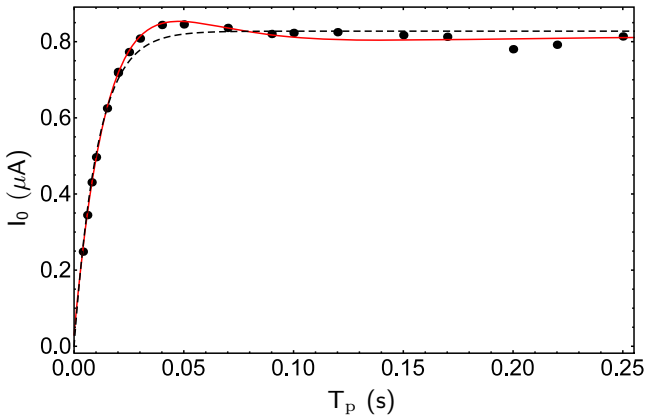

Fig. 3. Dependence of the FSP amplitude $I_0 = \sqrt{I_c^2 + I_s^2}$ on the pumping time T_p with a pump power P_p of 40 μA, a duty cycle η of 30% (determined to be optimal in an auxiliary experiment) and a readout power P_r of 1 μA.

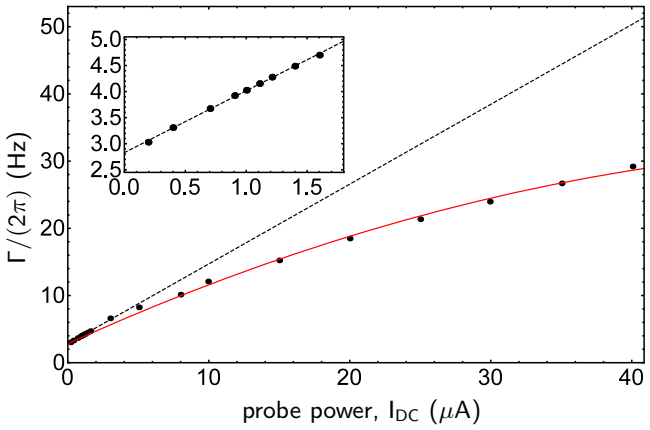

Fig. 4. Effective FSP relaxation rate $\Gamma = \gamma + \gamma_r$ as function of probe power P_r, represented by the DC photocurrent I_{DC}. The solid (red) line represents a second-order polynomial fit, the linear part of which is shown as dashed (black) line. The inset shows the range of low probe powers that are relevant for the FSP-magnetometer operation. The intrinsic relaxation rate, i.e. $\Gamma(\gamma_r \to 0)$, is $\gamma/(2\pi) = 2.83(2)$ Hz.

5.3 Performance in the shotnoise limit

The effective relaxation rate $\Gamma = \gamma + \gamma_r$ depends, via γ_r (residual pump rate during the probing phase) in a linear manner on the probe power P_r. The data in Figure 4 demonstrate that this linear dependence is obeyed for $\gamma_r < \gamma$. The saturation behaviour observed for larger probe power levels originates from the creation of higher order atomic polarization moments [33] that are not taken in account by our model that considers only vector polarization. Large readout power levels ($\gamma_r \gg \gamma$) increase the correction factor C, while low probe power levels ($\gamma_r \ll \gamma$) reduce the signal to noise ratio I_0/ρ_I of the detected FSP.

Based on the above, one expects the magnetometric noise density ρ_{B_0} to exhibit a minimum as a function of probe power. The data in the lower part of Figure 5 demonstrate that the probe power dependence of ρ_{B_0} (evaluated in the shotnoise limit) shows indeed a shallow

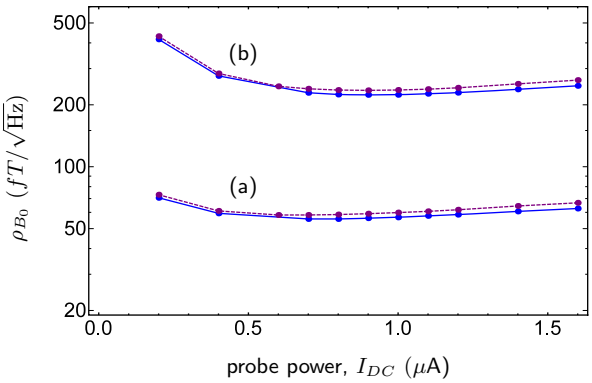

Fig. 5. Shotnoise-limited magnetometer sensitivity as a function of probe power (measurement time $T = 100$ ms, duty cycle 30%), assuming photocurrent-shotnoise-limited performance (a) and with real world noise (b). In both graphs the blue (solid) and purple (dashed) lines represent results obtained with pump power values P_p of 30 and 15 μA, respectively.

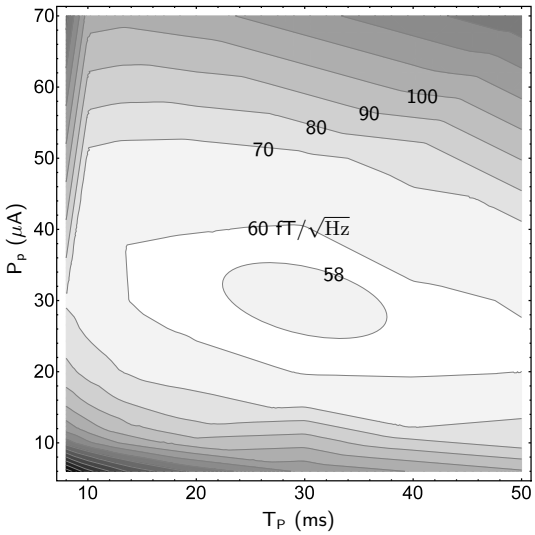

Fig. 6. Dependence of the shotnoise limited magnetometric sensitivity on the pumping time T_p and the pump power P_p. The measurement time was 100 ms, the probe power 1 μA and the pump duty cycle $\eta = 30\%$. The experimentally determined minimum of ρ_{B_0} is below 60 fT/$\sqrt{\text{Hz}}$ in the shotnoise limit.

minimum for $\gamma_r \approx \gamma$. The displayed ρ_{B_0} values were calculated from equations (13), (16) and (14) using as input parameters the experimentally determined values of I_0 and Γ as well as the set value of T_r, while the spectral noise density ρ_I in (13) was taken to be the shotnoise value, $\rho_I = \sqrt{2eI_{DC}}$ of the DC photocurrent I_{DC}.

Figure 6 shows contour plots of constant ρ_{B_0} values as a function of the pump power P_p and pumping time T_p, assuming shotnoise-limited detection with a probe power P_r of 1 μA. The elongated region of best sensitivity along the T_p-direction reflects the saturation behaviour of Figure 3. We note that the pump power of ≈30 μA required for optimal performance is ∼ 10 times larger than the optimal

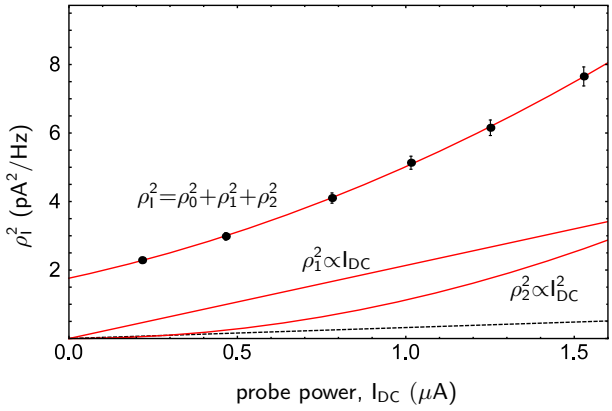

Fig. 7. Probe power dependence of the spectral noise power density ρ_I^2 of the signal as estimated from the FFT of the signal (black dots). The signal was sampled at 6.25 MHz with a 16 bit resolution. The individual contributions $\rho_1^2 = \alpha_1 I_{DC}$, and $\rho_2^2 = \alpha_2 I_{DC}^2$ are shown below. The fit parameters are $\rho_0^2 = 1.76(6)$ pA^2/Hz, $\alpha_1 = 2.13(15)$ pA^2/(μA Hz), and $\alpha_2 = 1.76(6)$ pA^2/(μA^2 Hz). The line connecting the experimental data points represents a linear regression $\sigma_\alpha^2 = 1.12(9)I_{DC}^2 + 2.13(15)I_{DC} + 1.76(6)$ pA^2/Hz. The dashed (black) line presents the theoretical lower limit of the σ_α^2 given by the shotnoise $2eI_{DC}$.

power for operating the same vapor cell in the M_x magnetometer mode [10] using cw light.

5.4 Real world magnetometer performance

The FSP magnetometer's performance shown in Figures 5 and 6 is based on experimental parameters, assuming the spectral noise density ρ_I to be given by the shotnoise of the average photodiode current I_{DC} during the FSP recording time. In real experiments the noise level generally exceeds the fundamental shotnoise limit, sources of excess noise being technical noise of the laser power, frequency fluctuations of the laser (converted to signal amplitude fluctuations by the spectral line shape of the optical absorption line), intrinsic amplifier noise and noise from the analog/digital conversion process in the data acquisition system. The different noise contributions depend in a different manner on laser power, and a measurement of the power dependence of the signal noise density near the Fourier component of interest ($f_L = \omega_L/(2\pi)$) is useful for identifying different noise sources. The result of such a measurement is shown in Figure 7, together with a fit by a second order polynomial $\rho_I^2(I_{DC}) = \rho_0^2 + \rho_1^2 + \rho_2^2$. One sees that the magnetometer noise has a large I_{DC}-independent contribution ρ_0^2 of ≈1.7 pA^2/Hz, which we believe to originate from digitization noise that results from the interplay of the 16 bit digitizer and the 6.25 MHz sample rate. The contributions ρ_1^2 and ρ_2^2 are proportional to I_{DC} and I_{DC}^2, respectively. While the contribution $\rho_2 \propto I_{DC}$ represents technical laser power noise, the contribution ρ_1 is expected to represent the shotnoise ($\rho_1 \propto \sqrt{I_{DC}}$) of the photocurrent. The data in Figure 7 show that the latter contribution is ∼6 times larger than the anticipated shotnoise

contribution of $\rho_1 = \sqrt{2eI_{DC}}$. The mentioned digitization noise may also be responsible for this excess noise, and planned future experiments with a higher resolution digitizer may shine more light on this.

Knowing the experimental dependence of ρ_I on the probe power I_{DC} we can represent the dependence of the real-world magnetometer sensitivity on the probe power. This result is represented by the upper traces in Figure 5, from which we may claim that our present FSP magnetometer is able to measure magnetic field changes below 250 fT with a detection bandwidth of 1 Hz or, equivalently, a recording time of 0.5 s.

6 Precision and accuracy

The shotnoise-limited sensitivity of the FSP magnetometer reported above is typically a factor of 10 worse than the sensitivity achieved with a feedback-driven M_x magnetometer using the same cell at the same temperature [22]. The duty cycle of the FSP mode of operation, in which preparation alternates with readout (actual measurement) contributes a degradation factor of ∼1.5 to this effect. To this add contributions from the lower readout power and signal damping in the FSP mode compared to the continuous operation mode. It is precisely this aspect which motivated the research described here. Many atomic magnetometry applications, such as the recording of magnetic fields for biomedical purposes [2–4,6] call for magnetometers with the highest possible sensitivity, i.e., the best capability to detect small magnetic field changes. For such applications, the accuracy of the field determination is of secondary importance.

In our collaborative effort searching for a permanent electric dipole moment of the neutron [8] an array of Cs M_x-magnetometers monitors the spatial and temporal evolution of the magnetic field applied to an ensemble of ultracold neutrons, a task, for which sensitivity is a primary issue. However, the control of systematic effects in that experiment requires the control of magnetic field gradients, derived from readings of two magnetometers located at different positions. An accurate gradient determination sets severe constraints on the precision of those readings.

Precision limitation of M_x-magnetometer

In an M_x-magnetometer a continuous oscillation at the Larmor frequency is sustained by active feedback [9,10]. In more detail: atomic spin polarization created by optical pumping is made to precess around the magnetic field $\boldsymbol{B}_0$ of interest by driving the magnetization with a weak magnetic field $\boldsymbol{B}_1(t)$ oscillating at frequency ω_{rf} in a direction perpendicular to $\hat{B}_0$ or rotating at that frequency around $\hat{B}_0$ in a plane orthogonal to the field. As a consequence the transmitted light intensity oscillates at the frequency ω_{rf}, the phase relation between the light modulation and the rf-drive being those of a classical harmonic oscillator (Fig. 8). On resonance the two oscillations

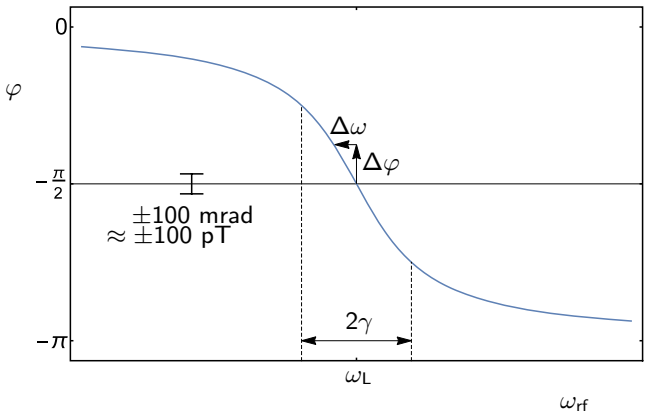

Fig. 8. Phase between rf excitation and optical response in an M_x-magnetometer that is used for the magnetometer's feedback operation. The linear dependence near resonance extends over a range of ±100 pT (for a linewidth $\gamma/(2\pi)$ of 3.5 Hz), over which the magnetometer has a maximal sensitivity. When an accuracy of ∼100 fT is sought, the phase has to be locked to $\varphi = -\pi/2$ with a precision of ∼10 fT.

are dephased by –90°, and near resonance ($\omega_{rf} \approx \omega_L$) the phase obeys

$$\varphi \approx -\frac{\pi}{2} - \frac{\delta\omega}{\gamma} = -\frac{\pi}{2} - \frac{\omega_{rf} - \omega_L}{\gamma}. \qquad (17)$$

This linear dependence is used as a discriminator in a feedback loop that actively locks ω_{rf} to ω_L.

In order to yield accurate measurement results, the feedback loop has to assure that the phase is precisely locked to $\varphi = -\pi/2$. A sought accuracy ΔB, say of 10 fT, requires a phase control $\Delta\varphi = \gamma_F \Delta B/\gamma$ of 10 μrad, assuming a relaxation rate of $\gamma = 2\pi\,3.5$ Hz. Even if this precision in the phase setting may be achieved – noting, en passant, the requirement of a phase detector with at least 17 bit resolution to achieve this – it will be practically impossible to guarantee its stability, thinking, e.g., of temperature dependent impedance changes in the feedback circuitry.

From Figure 8 one sees that the discriminator function is linear in a range of ±100 mrad near resonance, corresponding to several 100 pT, and the magnetometer will keep its high sensitivity, when the phase is locked within that range. An M_x-magnetometer may thus be able to measure field changes in the lower fT range, while its absolute field reading may be wrong in the upper pT range.

The Bloch-Siegert shift [34] is a major source for systematic readout errors in M_x-magnetometers. For practical reasons the rf field used to drive the magnetic resonance is usually laid out as an oscillating, rather than a rotating field. In the rotating wave approximation, one considers only the rf field component that corotates with the polarization around $\hat{B}_0$. The neglected counter-rotating field shifts the magnetometer's oscillation frequency by the Bloch-Siegert shift δB_{BS} on the order of $\approx\gamma/2Q$, where Q is the resonance's quality factor. As an example the Cs magnetic resonance frequency in

a 1 μT field ($\omega_L/(2\pi) = \nu_L = 3.5$ kHz), measured with a 5 Hz linewidth, has a Q-factor of 700, thus shifting the resonance by $\delta\nu_{BS} = 3.6$ mHz, corresponding to a readout error on the order of 1 pT.

7 Systematic effects in an FSP magnetometer

Since the FSP magnetometer described here records the free precession of the Cs spin polarization it is not subject to the above systematic shifts associated with driving the resonance in a feedback mode. Nonetheless, its precision and accuracy are affected by several systematic readout errors that we address below. To note that some of these systematic effects will also affect the M_x magnetometer, in addition to the effects discussed above.

7.1 Light shift

It is well-known that circularly-polarized light may induce a magnetic sublevel shift that is proportional to the optical pumping rate γ_r, itself proportional to the intensity of the readout light beam. This level shift has the same characteristics as the shift induced by a magnetic field directed along the laser propagation direction $\boldsymbol{k}$, so that the light-induced shift can be expressed in terms of an effective field $\boldsymbol{b}_{LS} = b_{LS}\hat{k}$. The effect vanishes when the laser frequency is tuned exactly to the center of the optical absorption line, and for a laser frequency that is slightly ($\delta\omega_{opt} \ll \Gamma_D$) detuned from the line center the light shift reads $b_{LS} \approx (\delta\omega_{opt}/\Gamma_D)(\gamma_r/\gamma_F)$, where Γ_D is the Doppler width of the optical transition. For $\Gamma_D/(2\pi) \approx 300$ MHz, $\delta\omega_{opt}/(2\pi) = 0.3$ MHz and $\gamma_r/(2\pi) = 3.5$ Hz one has $b_{LS} \approx 1$ pT. Noting that $\boldsymbol{b}_{LS}$ is nominally perpendicular to $\boldsymbol{B}_0$, which implies, for a 1 μT field, a shift of $\delta B_{LS} = |\boldsymbol{B}_0 + \boldsymbol{b}_{LS}| - B_0 \approx b_{LS}^2/2B_0$ that is below 10^{-18} T and thus completely negligible for any practical application.

7.2 Quadratic Zeeman effect

In very low magnetic fields the magnetic-field-induced energy spacing of adjacent magnetic sublevels $|F_g, m_{F_g}\rangle$ and $|F_g, m_{F_g} - 1\rangle$ are all equal and proportional to B_0. In this linear Zeeman regime, a magnetic resonance transition between magnetic sublevels of the hyperfine ground state level F_g consists of $2F_g$ degenerate overlapping lines that represent the $2F_g$ magnetic resonance transitions $|F_g, m_{F_g}\rangle \rightarrow |F_g, m_{F_g} - 1\rangle$ between ground state magnetic sublevels. In larger fields the sublevel spacings acquire – by virtue of the Breit-Rabi interaction – an m_F^2 dependent change that is proportional to B_0^2. This quadratic Zeeman effect (QZE) lifts the degeneracy of the overlapping lines, which manifests itself (in the general case) in an asymmetrically-broadened magnetic resonance line, assuming that quadratic shifts to be smaller than the linewidths of the individual components. As a consequence the center frequency of the magnetic resonance shifts, leading to a magnetometric readout error, when the resonance center frequency is used (as is the case with both the FSP and the M_x magnetometers) to infer the field value. The quantitative value of this shift depends on the degree (and nature, i.e., vector vs. tensor) of the spin polarization created by optical pumping. In a 1 μT field the maximum QZE, i.e., the shift obtained with a 100% polarized sample, is on the order of 3 pT. Since this shift can be calibrated, it can be accounted for by a (field dependent) correction of the readout signal.

We note that the magnitude of the QZE-induced shift depends on the field orientation. We have verified that under ideal geometrical conditions, i.e., for $\boldsymbol{k} \perp \boldsymbol{B}_0$, the FSP magnetometer is not affected by the QZE (as expected from symmetry considerations), while the oscillation frequency of a readout beam propagating along a direction making an angle $\vartheta \neq \pi/2$ with the magnetic field is affected by a frequency shift that can be explained by the Breit-Rabi formula.

7.3 Imperfect light polarization

Last, but by far not least, we mention our (puzzling) observation that the purity of circular polarization of the readout beam is crucial for avoiding systematic readout errors. We found in fact that in an non-ideal geometry where $\boldsymbol{k} \not\perp \boldsymbol{B}_0$ – a small ellipticity of the laser beam's polarization (i.e., contamination by a finite degree of linear polarization) produces a readout error in the pT range for a $\sim$1 μT field. This effect and the quadratic Zeeman effect are currently under detailed study in our lab.

7.4 Magnetometer accuracy

With the exception of the effect associated with light polarization (that we are not yet in a position to quantify), all discussed systematic effects are either negligible or can be corrected for when the system parameters are known. The FSP magnetometer can thus have an accuracy that is comparable to its shotnoise-limited sensitivity. Since the field determination relies on a frequency measurement, the gyromagnetic ratio γ_F plays the role of an atomic calibration constant and the accuracy of any inferred field value will be limited by the precision of the numerical value of γ_F. The gyromagnetic ratio of the $F_g = 4$ hyperfine level of the $6^2S_{1/2}$ Cs ground state used in the FSP magnetometer has the experimental value of $\gamma_4 = 2\pi\, 3.49862110(36)$ Hz/nT that can be derived from the ground state's electronic (g_J) and nuclear (g_I) Landé factors [35]. The relative uncertainty $\Delta\gamma_F/\gamma_F$ of $\sim 10^{-7}$ therefore limits the absolute accuracy of a $\sim$1 μT field determination to $\sim$100 fT, again comparable with the statistical uncertainty.

8 Summary and conclusion

We have presented an atomic magnetometer based on the free spin precession of orientation in the $F_g = 4$ hyperfine ground state of Cs atoms contained in a paraffin-coated

cell at room temperature. We have optimized the experimental parameters (power, duty cycle and duration of the pump process as well as the readout power and duration) in order to achieve an optimal magnetometric sensitivity $\Delta B_0^{0.5\ \mathrm{s}}$ with a 0.5 s total measurement time.

Under optimized conditions the magnetometer has a shotnoise-limited sensitivity $\rho_{B_0} < 60\,\mathrm{fT}/\sqrt{\mathrm{Hz}}$, which represents the average fluctuation of 5 subsequent FSP signals cycles, each one 100 ms duration. Our real-world experiment yielded a sensitivity of $\approx$200 $\mathrm{fT}/\sqrt{\mathrm{Hz}}$. The sensitivity may be enhanced by shortening the pumping time using a spectrally broader laser beam (in combination, eventually with a repumper), and expanding the laser beam to fill the whole cell.

We have addressed several systematic effects that may affect the magnetometer's absolute accuracy and cannot identify any effect that would lead to an accuracy above the current (200 $\mathrm{fT}/\sqrt{\mathrm{Hz}}$) or shotnoise limited (60 $\mathrm{fT}/\sqrt{\mathrm{Hz}}$) sensitivity of the magnetometer. We note, however, that the last statement is only valid under ideal conditions, viz., $\boldsymbol{k} \perp \boldsymbol{B}_0$. We stress that an unexpected – so far unexplained – large frequency shift occurs when this condition is violated. It is very likely that the latter effect is not present in FSP magnetometers operated with linearly polarized light, i.e., detection of the free spin precession of atomic alignment. So far no quantitative studies of the accuracy of alignment-based FSP magnetometers has been performed.

Note also, that in a $B_0 = 1\ \mu$T field, the relative sensitivity $\Delta B_0^{0.5s}/B_0$ is of the same order of magnitude as the relative accuracy of the gyromagnetic ratio γ_4 of the $F_g = 4$ state.

We feel that FSP magnetometry will be useful for the precise measurement of ratios of gyromagnetic factors [36] in different atoms, such as Cs, ^{3}He, ^{4}He, Hg, Rb etc. We also propose to deploy an array of FSP magnetometers as the one described here (or an extension towards aligned atoms) for measuring and monitoring the spatial field distribution in experiments relying on accurate field determinations, such as nEDM experiments. All sensors of the array may be driven by beams derived from a single laser, using only a single EOM. The all-optical feature implies the absence of any galvanic connection to the sensor heads, easing the operation in harsh environments (vacuum, underwater, or near high voltage electrodes), providing that the light to the sensor head and from the head to the photodetector is carried by optical fibers.

This work was supported by the grant 200020_140421/1 of the Swiss National Science Foundation. We are grateful to H.-C. Koch and M. Kasprzak for useful comments and discussions.

References

1. D. Budker, M. Romalis, Nat. Phys. **3**, 227 (2007)
2. G. Bison, N. Castagna, A. Hofer, P. Knowles, J. Schenker, M. Kasprzak, H. Saudan, A. Weis, Appl. Phys. Lett. **95**, 173701 (2009)
3. R. Wyllie, M. Kauer, R. Wakai, T. Walker, Opt. Lett. **37**, 2247 (2012)
4. C. Johnson, P. Schwindt, M. Weisend, Phys. Med. Biol. **58**, 6065 (2013)
5. P. Ganssle, H. Shin, S. Seltzer, V. Bajaj, M. Ledbetter, D. Budker, S. Knappe, J. Kitching, A. Pines, Angew. Chem. Int. Ed. **53**, 9766 (2014)
6. I. Savukov, T. Karaulanov, C. Wurden, L. Schultz, J. Mag. Res. **233**, 103 (2013)
7. C. Baker, D. Doyle, P. Geltenbort, K. Green, M. van der Grinten, P. Harris, P. Iaydjiev, S. Ivanov, D. May, J. Pendlebury, J.D. Richardson, D. Shiers, K.F. Smith, Phys. Rev. Lett. **97**, 131801 (2006)
8. I. Altarev, G. Ban, G. Bison, K. Bodek, M. Burghoff, M. Cvijovic, M. Daum, P. Fierlinger, E. Gutsmiedl, G. Hampel, W. Heil, R. Henneck, M. Horras, N. Khomutov, K. Kirch, St. Kistryn, S. Knappe-Grüuneberg, A. Knecht, P. Knowles, A. Kozela, J.V. Kratz, F. Kuchler, M. Kuzniak, T. Lauer, B. Lauss, T. Lefort, A. Mtchedlishvili, O. Naviliat-Cuncic, S. Paul, A.S. Pazgalev, G. Petzoldt, E. Pierre, C. Plonka-Spehr, G. Quéméner, D. Rebreyend, S. Roccia, G. Rogel, T. Sander-Thoemmes, A. Schnabel, N. Severijns, Yu. Sobolev, R. Stoepler, L. Trahms, A. Weis, N. Wiehl, J. Zejma, G. Zsigmond, Nucl. Instr. Meth. Phys. Res. A **611**, 133 (2009)
9. G. Bison, R. Wynands, A. Weis, J. Opt. Soc. Am. B. **22**, 77 (2005)
10. S. Groeger, G. Bison, J.L. Schenker, R. Wynands, A. Weis, Eur. Phys. J. D **38**, 239 (2006)
11. H. Dehmelt, Phys. Rev. Lett. **105**, 1924 (1957)
12. S. Kukolich, Am. J. Phys. **36**, 919 (1968)
13. C. Bowers, G. Wäckerle, M. Mehring, Phys. Rev. A **46**, 7042 (1992)
14. J. Skalla, S. Lang, G. Wäckerle, J. Opt. Soc. Am. B **12**, 772 (1995)
15. K. Green, P. Harris, P. Iaydjiev, D. May, J. Pendlebury, K. Smith, M. van der Grinten, P. Geltenbort, S. Ivanov, Nucl. Instr. Meth. Phys. Res. A **404**, 381 (1998)
16. A. Nikiel, P. Blümler, W. Heil, M. Hehn, S. Karpuk, A. Maul, E. Otten, L. Schreiber, M. Terekhov, Eur. Phys. J. D **68**, 330 (2014)
17. H.-C. Koch, G. Bison, Z. Grujic, M. Kasprzak, P. Knowles, A. Weis, W. Heil, A. Kraft, A. Pazgalev, A. Schnabel, J. Voigt, e-print [arXiv:1502.06366]
18. S. Seltzer, P. Meares, M. Romalis, Phys. Rev. A **75**, 051407 (2007)
19. L. Lenci, S. Barreiro, P. Valente, H. Failache, A. Lezama, J. Phys. B **45**, 215401 (2012)
20. L. Lenci, A. Auyuanet, S. Barreiro, P. Valente, A. Lezama, H. Failache, Phys. Rev. A **89**, 043836 (2014)
21. E. Breschi, Z. Grujić, A. Weis, Appl. Phys. B **115**, 85 (2014)
22. N. Castagna, G. Bison, G. Domenico, A. Hofer, P. Knowles, C. Macchione, H. Saudan, A. Weis, Appl. Phys. B **96**, 763 (2009)
23. W. Bell, A. Bloom, Phys. Rev. Lett. **6**, 280 (1961)
24. W. Gawlik, L. Krzemien, S. Pustelny, D. Sangla, J. Zachorowski, M. Graf, A.O. Sushkov, D. Budker, Appl. Phys. Lett. **88**, 131108 (2006)
25. V. Schultze, R. IJsselsteijn, T. Scholtes, S. Woetzel, H. Meyer, Opt. Exp. **20**, 14201 (2012)

26. Z. Grujić, A. Weis, Phys. Rev. A **88**, 012508 (2013)
27. K. Jensen, V. Acosta, J. Higbie, M. Ledbetter, S. Rochester, D. Budker, Phys. Rev. A **79**, 023406 (2009)
28. N. Castagna, A. Weis, Phys. Rev. A **84**, 053421 (2011)
29. N. Castagna, A. Weis, Phys. Rev. A **85**, 059907 (2012)
30. H. Cramér, *Mathematical Methods of Statistics* (Princeton University Press, 1946)
31. C. Rao, Bull. Calcutta Math. Soc. **37**, 81 (1945)
32. C. Gemmel, W. Heil, S. Karpuk, K. Lenz, C. Ludwig, Y. Sobolev, K. Tullney, M. Burghoff, W. Kilian, S. Knappe-Grüneberg, W. Müuller, A. Schnabel, F. Seifert, L. Trahms, St. Baeßler, Eur. Phys. J. D **57**, 303 (2010)
33. D. Budker, W. Gawlik, D. Kimball, S. Rochester, V. Yashchuk, A. Weis, Rev. Mod. Phys. **74**, 1153 (2002)
34. F. Bloch, A. Siegert, Phys. Rev. **57**, 522 (1940)
35. E. Arimondo, M. Inguscio, P. Violino, Rev. Mod. Phys. **49**, 31 (1977)
36. S. Afach, C. Baker, G. Ban, G. Bison, K. Bodek, M. Burghoff, Z. Chowdhuri, M. Daum, M. Fertl, B. Franke, P. Geltenbort, K. Green, M.G.D. van der Grinten, Z. Grujic, P.G. Harris, W. Heil, V. Hlaine, R. Henneck, M. Horras, P. Iaydjiev, S.N. Ivanov, M. Kasprzak, Y. Kermadic, K. Kirch, A. Knecht, H.-C. Koch, J. Krempel, M. Kuniak, B. Lauss, T. Lefort, Y. Lemire, A. Mtchedlishvili, O. Naviliat-Cuncic, J.M. Pendlebury, M. Perkowski, E. Pierre, F.M. Piegsa, G. Pignol, P.N. Prashanth, G. Qumner, D. Rebreyend, D. Ries, S. Roccia, P. Schmidt-Wellenburg, A. Schnabel, N. Severijns, D. Shiers, K.F. Smith, J. Voigt, A. Weis, G. Wyszynski, J. Zejma, J. Zenner, G. Zsigmond, Phys. Lett. B **739**, 128 (2014)